

Composition of an Emission Line System in Black Hole Host Globular Cluster RZ2109

Matthew M. Steele^{1,2}, Stephen E. Zepf¹, Thomas J. Maccarone³, Arunav Kundu⁴, Katherine L. Rhode⁵, and John J. Salzer⁵

ABSTRACT

We present an analysis of optical spectra from the globular cluster RZ2109 in NGC 4472, which hosts the first unambiguous globular cluster black hole. We use these spectra to determine the elemental composition of the emission line system associated with this source, and to constrain the age and metallicity of the host globular cluster. For the emission line system of RZ2109, our analysis indicates the [O III] λ 5007 equivalent width is $33.82 \pm 0.39 \text{ \AA}$ and the H β equivalent width is $0.32 \pm 0.32 \text{ \AA}$, producing a formal [O III] λ 5007/H β emission line ratio of 106 for a 3200 km s^{-1} measurement aperture covering the full velocity width of the [O III] λ 5007 line. Within a narrower 600 km s^{-1} aperture covering the highest luminosity velocity structure in the line complex, we find [O III] λ 5007/H β = 62. The measured [O III] λ 5007/H β ratios are significantly higher than can be produced in radiative models of the emission line region with solar composition, and the confidence interval limits exclude all but models which have gas masses much larger than those for a single star. Therefore, we conclude that the region from which the [O III] λ 5007 emission originates is hydrogen-depleted relative to solar composition gas. This finding is consistent with emission from an accretion-powered outflow driven by a hydrogen-depleted donor star, such as a white dwarf, being accreted onto a black hole.

1. INTRODUCTION

The globular cluster RZ2109 located in the galaxy NGC4472 is a known host of an accreting black hole system, first identified by Maccarone et al. (2007). Along with the variable X-ray source indicative of the accreting black hole, RZ2109 has been observed to host a broad and luminous

¹Department of Physics & Astronomy, Michigan State University, East Lansing, MI 48824; e-mail: steele24@msu.edu

²Department of Physics, Northern Michigan University, Marquette, MI 49855

³Department of Physics, Texas Tech University, Lubbock, TX 79409

⁴Eureka Scientific, 2452 Delmer Street Suite 100, Oakland, CA 94602-3017

⁵Department of Astronomy, Indiana University, Bloomington, IN 47405

[O III] $\lambda\lambda$ 4959,5007 emission line complex thought to correspond to an accretion-powered outflow driven from the cluster’s black hole (Zepf et al. 2007, 2008; Steele et al. 2011).

The RZ2109 emission line structure is unusual in many respects. The lines are very broad with a width of 3200 km s^{-1} , about a factor of 100 larger than the escape velocity of the globular cluster in which it is located. The line velocity profiles also have a complex shape and appear to contain two distinct velocity structures (Steele et al. 2011). Moreover, [O III] $\lambda\lambda$ 4959,5007 are the only emission lines apparent even in a fairly deep spectrum (Zepf et al. 2008). Gnedin et al. (2009) suggested that the lack of Balmer line emission, in particular, may be indicative of a hydrogen poor donor star such as a white dwarf. This possibility is significant because although BH-WD binaries are an expected end stage of stellar evolution, especially in globular clusters, none has yet been positively identified (Ivanova 2011).

A common diagnostic for the study of emission line regions is the [O III] λ 5007/ $H\beta$ emission line ratio. Previous work by Zepf et al. (2008) noted that [O III] λ 5007/ $H\beta$ ratio appeared to be at least 30 based on a low resolution optical spectrum of the RZ2109 cluster. For reference other common astrophysical [O III] emission line production sites include active galactic nuclei with typical [O III] λ 5007/ $H\beta$ ratios of order unity (Sarzi et al. 2006), Milky Way planetary nebulae with mean line ratios of approximately 15 (Stanghellini et al. 2003), and a few extremely hydrogen poor planetary nebulae with line ratio of 20 (Méndez et al. 2005; Larsen 2008). Based on a comparison to these sources, it seems plausible that the RZ2109 emission line site would be hydrogen-depleted. On the other hand, the [O III] production sites and mechanisms can be very different among astrophysical object classes and it is not immediately obvious how relevant such comparisons are.

In this work we investigate the composition of the RZ2109 emission line region in order to help constrain models of the black hole/donor star binary in the globular cluster. Accordingly, Section 2 presents an analysis of higher signal-to-noise spectra of RZ2109 than have been previously used to explore the composition of the source. In Section 3, we begin by modeling the stellar component of the RZ2109 spectrum to remove the stellar contributions from the emission line measurements. The next section presents the line measurement results. Section 3.3 presents results from a suite of radiative models that we use to interpret the range of [O III] λ 5007/ $H\beta$ emission line ratios. The last section of the paper includes a discussion of the overall results of this analysis.

2. OBSERVATIONS AND DATA REDUCTION

The optical spectra used in this study were collected using the Gemini Multi Object Spectrograph (GMOS) on the Gemini South Telescope. These data, first presented in Steele et al. (2011), were taken on the consecutive nights of UT 2009 March 28–29 (program GS-2009A-Q-1). The medium resolution spectra ($R \sim 2400$) have a wavelength coverage from 4445–6023 Å. The data were reduced using the longslit tools in the Gemini IRAF package. One dimensional spectra were extracted from the processed spectra and, following tests to ensure the emission line object was not

varying between nights (Steele et al. 2011), co-added to increase the signal-to-noise ratio.

The resulting reduced spectrum is a superposition of the emission line source of interest and the stellar component of the host globular cluster. In order to examine the emission line source in isolation, the stellar component must be modeled and removed.

3. ANALYSIS AND RESULTS

3.1. Stellar Component Modeling

The modeling of the stellar component was performed in a process similar to that described in Steele et al. (2011). The RZ2109 Gemini spectrum was fit to a grid of continuum normalized synthetic spectra constructed using the Pegasé-HR code of Le Borgne et al. (2004) and Elodie 3.1 (Prugniel et al. 2007) stellar library. A Kroupa IMF (Kroupa 2001) was adopted along with a single epoch of star formation to construct the synthetic stellar population grid using cluster age and initial metallicity as free parameters. To avoid emission lines contaminating the fit with the inclusion of emission lines with non-stellar origins, the region between 4870–5060 Å in the observed frame (4846–5035 Å rest frame) was masked out to exclude contributions from $H\beta$ and $[O\ III]\lambda 5007$ to the χ^2 minimization fitting scheme. The resulting best-fit stellar model corresponded to an age of 13.25 Gyr and a metallicity of $[Fe/H] = -1.0$.

The best-fitting synthetic stellar population model provides, qualitatively, an excellent match to the stellar component of the observed spectrum of RZ2109. Figure 1 provides a comparison between the observed spectrum and the best-fit model over the entire spectral wavelength range, along with an inset showing the $H\beta$ region in detail.

In order to determine the uncertainties in the fitted parameters, simulated observations were performed by constructing a best-fit synthetic stellar component spectrum and injecting noise to match the signal-to-noise of the observations. The simulated observation was then fit to produce a new set of stellar parameters. This simulated observation process was performed for 10^5 iterations with the resultant probability density distribution of the stellar component parameter fits shown in Figure 2. From this exercise it is evident that the fit is well constrained in $[Fe/H]$, while displaying a greater spread in the age parameter. Some of the observed spread in age results from the exclusion of $H\beta$, the feature most sensitive to age, in the fitting scheme. The log scale used for the stellar parameter density distribution in Figure 2 may overemphasize the spread in age; only 1 percent of the simulated observations had age determinations below 5.75 Gyr and only 10 percent were below 8.50 Gyr. The adopted stellar parameters and associated uncertainties (Age = 13.25 ± 1.00 Gyr, $[Fe/H] = -1.0 \pm 0.1$) include 83 percent of all simulated observations in age and 98 percent in metallicity.

3.2. Equivalent Widths

The emission line’s equivalent widths (EW) are measured by direct integration of the continuum normalized spectrum bounded by a given velocity aperture. A second measurement is then performed over the identical aperture on the stellar model and the value subtracted from the data measurement in order to remove the influence of stellar absorption features. Given the complexity of the [O III] λ 5007 line profile the specification of the velocity aperture is non-trivial. Steele et al. (2011) find that the [O III] λ 5007 emission line in RZ2109 is well described by two components; a broad component with a width at zero intensity of $\sim 3200 \text{ km s}^{-1}$ and narrower component with a FWHM of $\sim 300 \text{ km s}^{-1}$. Here we perform measurements for apertures of two widths which correspond to the two components identified by Steele et al. (2011); a broad 3200 km s^{-1} aperture and a 600 km s^{-1} aperture. For reference the apertures over which the measurements are performed are plotted for the $\text{H}\beta$ and [O III] λ 5007 lines in figure 3. Table 1 gives the resulting measurements for [O III] λ 5007 and $\text{H}\beta$ in both the 3200 km s^{-1} apertures. The [O III] λ 5007/ $\text{H}\beta$ emission line ratios for each velocity aperture are very large (105.7 for the 3200 km s^{-1} aperture, 61.6 for the 600 km s^{-1} aperture), notably larger than found in previous measurements using lower signal-to-noise data (Zepf et al. 2008). This increase in the emission line ratios may be attributable solely to the higher signal-to-noise of the current data providing lower $\text{H}\beta$ measurement uncertainties, and therefore higher line ratios, rather than a change in the line luminosities of the source.

The cited 1σ uncertainties provide an estimate of the RMS uncertainties derived from the local continuum and Poisson statistic uncertainties for emission above the local continuum. To construct an estimate of the local continuum RMS two regions, one blueward, one redward, with a width equal to that of the measurement aperture were evaluated to find the mean expected deviations from the local continuum. The second uncertainty cited for the 600 km s^{-1} aperture $\text{H}\beta$ measurement reflects the uncertainty produced by the fit of the synthetic stellar population model. This uncertainty estimate was produced by injecting noise consistent with that of the observations into a synthetic stellar model with parameters matching the best-fit model, refitting the resulting spectrum with a new stellar model using the procedure described in Section 3.1, and remeasuring the $\text{H}\beta$ EW.

The contours plotted in Figure 2 display the $\text{H}\beta$ EW as a function of the stellar component parameters. The unit label for each contour is given as a multiple of the 600 km s^{-1} aperture EW measurement of the best-fit stellar parameter model. Considering the full stellar parameter space covered by the simulated observations detailed in Section 3.1, the mean $\text{H}\beta$ EW of the simulated observations is two percent greater than the cited value for the 600 km s^{-1} aperture of 0.21 \AA , with 58 percent of the iterations falling within 10 percent and 89 percent of iterations within 20 percent of the cited value. If we limit consideration to only those simulated observations located within the uncertainty bounds of the best-fit stellar parameters, the mean $\text{H}\beta$ EW is one percent less than the cited value, 66 percent of iterations are within 10 percent of the cited value and all simulated observations are within 20 percent. Therefore an uncertainty in the 600 km s^{-1} aperture $\text{H}\beta$ EW measurement of 20 percent is adopted.

The uncertainty estimates of the $[\text{O III}]\lambda 5007/\text{H}\beta$ emission line ratios are dominated by uncertainties in the $\text{H}\beta$ measurement. For small values of $\text{H}\beta$ the discontinuity in the $[\text{O III}]\lambda 5007/\text{H}\beta$ ratios, $[\text{O III}]\lambda 5007/\text{H}\beta$ goes to infinity as $\text{H}\beta$ goes to zero, complicates the interpretation of uncertainties expressed in the conventional format. For example, the 3200 km s^{-1} aperture emission line ratio is $105.7_{-52.9}^{+\infty}$. For clarity it is helpful to consider the uncertainties of the $[\text{O III}]\lambda 5007/\text{H}\beta$ ratio in terms of limits at set confidence intervals, as expressed in Figure 3. Further discussion of these limits and there interpretation is included in Section 4.

It should be noted that ratios of emission line EW are not always directly comparable to ratios of emission line fluxes. EWs are measured relative to the local continuum level, thus two emission lines with equal flux values will only have equal EW values if the continuum level is the same at each lines observed wavelength. In the case of RZ2109 measurements of the flux calibrated continuum at the observed line-center of $[\text{O III}]\lambda 5007$ and $\text{H}\beta$ differ by ~ 1 percent, indicating that the $[\text{O III}]\lambda 5007/\text{H}\beta$ EW ratio is functionally equivalent (within measurement uncertainties) to a flux ratio.

Additional measurements were performed for a selection of other emission lines which the synthetic spectral modeling of Section 3.3 suggested may be present with EW a significant fraction of that of $\text{H}\beta$. These measurements were performed with a 600 km s^{-1} aperture on $\text{He II}\lambda 4686$ ($\text{EW} = 0.02 \pm 0.12$), $[\text{Ar IV}]\lambda 4740$ ($\text{EW} = 0.07 \pm 0.13$), and $[\text{Fe VII}]\lambda 5721$ ($\text{EW} = 0.07 \pm 0.08$). The uncertainties for these measurements reflect 1 sigma RMS deviations from the continuum, determined as describe above for the $[\text{O III}]\lambda 5007$ and $\text{H}\beta$ measurements. It should be noted that other than $[\text{O III}]\lambda 5007$ and the 600 km s^{-1} aperture $\text{H}\beta$ EW (which is a very weak detection), all EW for both 3200 and 600 km s^{-1} apertures are consistent with non-detections.

As the two emission components are thought to be produced in spatially and geometrically distinct structures, the emission line ratios derived using the two apertures need not be the same. Since the contributions of the broad and narrow emission components are superimposed, both the 3200 km s^{-1} or 600 km s^{-1} aperture measurements reflect an EW with contributions from both sources. In the 3200 km s^{-1} aperture the broad component dominates the EW, while the narrow component dominates in the 600 km s^{-1} aperture measurements. For reference, Steele et al. (2011) find that 81 percent of the total $[\text{O III}]\lambda 5007$ flux is contributed by the broad component and the remainder by the narrow component, though it should be noted deconvolving these contribution is necessarily a model-dependent calculation.

3.3. Emission Line System Modeling

In order to test the possibility that the measured $[\text{O III}]\lambda 5007/\text{H}\beta$ emission line ratios given above might be produced by a gas of solar composition, a series of radiative transfer models was constructed. The models were executed using version 08.01 of the Cloudy spectral synthesis code from Ferland et al. (1998).

The suite of models tested all had solar compositions and spherically symmetric shell gas distributions characterized by an inner and outer radius. The gas was assumed to be outflowing at a velocity of 300 km s^{-1} at the inner radius. The gas was gradually accelerated by radiation pressure from the X-ray source, increasing the velocity by a few percent at the outer radius. Under the prescription of an outflowing gas Cloudy adjusts the density to conserve mass flux (defined as the quantity $\rho(r)r^2u(r)$, where ρ is the gas density, u is the velocity, and r the radius) at each radius. The gas was irradiated by bremsstrahlung emission from a central source at 10^6 K , and normalized to match the X-ray luminosity observed by Shih et al. (2008) and Maccarone et al. (2007). Parameter space was then explored along the dimensions of the inner radius (R_0), hydrogen density at the inner radius ($\rho_H(R_0)$), and the total mass of the outflow. The free parameter space included in the model grid is summarized in Table 2. For each outflow mass range the limits on the inner radius and hydrogen density were selected to ensure the maximum [O III] $\lambda 5007/\text{H}\beta$ ratio model was surrounded by closed emission line ratio contours in parameter space. This criteria ensured that the maximum line ratio model identified at each outflow mass was a maximum in the local parameter space and not limited by the selection of boundary conditions.

As an example of the resultant model space for one specific outflow mass, Figure 4a displays the [O III] $\lambda 5007/\text{H}\beta$ emission line ratios for a model with a $0.2 M_\odot$ outflow as a function of R_0 and $\rho_H(R_0)$. Considering the case of a $0.2 M_\odot$ outflow allows us to investigate an interesting limit, since this is the minimum solar composition gas mass that can provide the $\sim 10^{-4} M_\odot$ of oxygen required to reproduce the observed [O III] emission (Steele et al. 2011). For this $0.2 M_\odot$ outflow a maximum emission line ratio of 26 occurs at $R_0 = 4.0 \times 10^{18} \text{ cm}$ and $\rho_H(R_0) = 1.0 \times 10^5 \text{ gm cm}^{-3}$.

The emission line ratio rises gradually with increased outflow mass reaching a maximum of [O III] $\lambda 5007/\text{H}\beta = 34$ near $10^2 M_\odot$ as seen in Figure 4b. The maximum emission line ratio for a range of outflow masses is given in Figure 5. The transition point in the maximum emission line ratio-mass ratio seen at a mass of 10^{34} g ($\sim 5 M_\odot$) occurs due to a change in the geometric distribution of the emitting gas that maximizes [O III] $\lambda 5007/\text{H}\beta$. For masses below the 10^{34} g threshold the optimal arrangement involves locating the gas in a thin shell ($R_0/\text{Thickness} \sim 10^5$) at a density which allows maximum [O III] $\lambda 5007$ emission across the shell. Above the threshold mass the optimal gas configuration is of a thicker distribution ($R_0/\text{Thickness} \sim 10^2$) and the [O III] $\lambda 5007$ emission is generated over a broad region located primarily in the half of the gas distribution most distant from the ionizing source. For reference in a recent study Peacock et al. (2012) find a half-light radius of 4-6 pc for the RZ2109 [O III] $\lambda 5007$ source, a few times greater than the outer radius producible by any solar composition model.

To evaluate the sensitivity of the [O III] $\lambda 5007/\text{H}\beta$ ratio on the input X-ray source temperature, a second model grid was calculated employing a higher temperature source. For an X-ray source temperature of $3 \times 10^6 \text{ K}$, the behavior of the maximum emission line ratio as a function of mass is largely similar to the $1 \times 10^6 \text{ K}$ case described above. The transition point seen produced by the shift in the optimal gas configuration occurs at a lower mass of $3 \times 10^{33} \text{ g}$, and the maximum [O III] $\lambda 5007/\text{H}\beta$ ratio of ~ 40 occurs near $30 M_\odot$. Over the range of masses evaluated the higher

temperature X-ray source produces line ratios 15–20 percent greater than the corresponding lower temperature model.

The outflow velocity of 300 km s^{-1} was selected to be broadly consistent with the observed 600 km s^{-1} feature, as the full observed width is produced by the superposition of approaching and receding flows. Increasing the velocity to 1600 km s^{-1} to match the observed boarder feature produces a minimal change in the resulting $[\text{O III}]\lambda 5007/\text{H}\beta$ ratio; on order of a few thousandths of a percent.

4. DISCUSSION AND CONCLUSION

From the EW measurements presented in Section 3.2 it is clear that any $\text{H}\beta$ emission which may be present in the observed RZ2109 spectrum is extremely weak. The $\text{H}\beta$ emission is sufficiently weak to make interpretation of the resulting $[\text{O III}]\lambda 5007/\text{H}\beta$ line ratios difficult. If taken at face value these ratios are among the largest detected from any astrophysical source (Sarzi et al. 2006; Méndez et al. 2005). In Table 3 the confidence levels for the $[\text{O III}]\lambda 5007/\text{H}\beta$ ratio are given based on the uncertainty in the $\text{H}\beta$ measurement. Equivalent width measurements below the level of the continuum (absorption features for example) are indicated with negative equivalent width value. Therefore a negative line ratio limit in Table 3 indicates that the $\text{H}\beta$ measurement is consistent with an absorption line at the specified confidence level.

When the full velocity width covered by the $[\text{O III}]\lambda 5007$ complex is considered along with the radiative transfer modeling presented in Section 3.3 it is clear that a solar composition gas is insufficient to produce the observed $[\text{O III}]\lambda 5007/\text{H}\beta$ ratios. The measured ratio using 3200 km s^{-1} apertures is nearly a factor of three larger than the maximum ratios produced by the synthetic emission line models. At the 95% confidence level for the 3200 km s^{-1} aperture and the 90% confidence level for the 600 km s^{-1} aperture the uncertainty limits on the $[\text{O III}]\lambda 5007/\text{H}\beta$ ratio approach the maximum synthetic $[\text{O III}]\lambda 5007/\text{H}\beta$ values. These ratio limits are 35.7 at 3200 km s^{-1} , and 33.0 at 600 km s^{-1} compared to the synthetic maximum of 34. As such it may be possible to produce the necessary $[\text{O III}]\lambda 5007/\text{H}\beta$ ratio for either aperture given an emission line region model that falls in a very specific location in physical parameter space. It should be noted, however, that the gas masses required to produce the maximum synthetic $[\text{O III}]\lambda 5007/\text{H}\beta$ values are well above what might be expected to be associated with an accreting black hole in a globular cluster. In order to produce the maximum synthetic $[\text{O III}]\lambda 5007/\text{H}\beta$ ratios a total gas mass of order $100 M_{\odot}$ is needed which would eliminate X-ray binaries, planetary nebulae, supernovae remnants, or any other stellar scale objects as the source of the emitting gas. To reach a gas mass of that size a significant portion of the gas would necessarily be contributed by the cluster’s interstellar medium. However the hydrogen densities involved in producing the maximum synthetic $[\text{O III}]\lambda 5007/\text{H}\beta$ ratios are of order $10^4\text{--}10^5 \text{ cm}^{-3}$, orders of magnitude above the expected densities of a cluster interstellar medium. Furthermore, the 10^{-1} solar composition of an interstellar medium would produce lower $[\text{O III}]\lambda 5007/\text{H}\beta$ ratios in comparison to the solar composition models considered

above, making a large contribution of ISM material to the emission line region unlikely. More typical gas masses produce maximum ratios a factor of four times smaller than those observed in the 3200 km s^{-1} aperture and nearly twice that of the lower limit of the 600 km s^{-1} measurement. The RZ2109 emission line region therefore appears to be oxygen enriched relative to solar composition.

The level of oxygen enrichment necessary to produce the observed $[\text{O III}]\lambda 5007/\text{H}\beta$ is not readily apparent, as the emission line systems physical parameters are not well constrained by observation. However, it is possible to examine some interesting limits by calculating the affect of carbon and oxygen enrichment for two characteristic masses; $1.0 M_{\odot}$ representing a stellar source of the emitting gas, and $0.1 M_{\odot}$ representing the outflow from a CO white dwarf and black hole binary. A grid of cloudy models, as described in section 3.3, was run for each characteristic mass with carbon and oxygen enriched from solar composition to 100 times solar. From this calculation we find a minimum CO enrichment of 17.8 times solar is necessary for the $1.0 M_{\odot}$ model to yield $[\text{O III}]\lambda 5007/\text{H}\beta$ ratios equivalent to the measured values of the 3200 km s^{-1} aperture and 5.5 times solar to match the 600 km s^{-1} aperture. For the $0.1 M_{\odot}$ model the gas must be enriched to 17.2 times solar for the 3200 km s^{-1} aperture and 5.6 times solar to match the 600 km s^{-1} aperture. We must emphasize that these are only lower limits on CO enrichment for two interesting astrophysical systems, and are not necessarily indicative of enrichment of the RZ2109 emission line source.

Steele et al. (2011) present the argument that the complex line $[\text{O III}]$ velocity profile observed in the RZ2109 spectrum is consistent with emission originating from two discrete gas structures. The two velocity apertures presented in this work do not directly correspond to the two geometric components discussed by Steele et al. (2011) as emission from the two components are superimposed in velocity space. From a comparison of the measured $[\text{O III}]\lambda 5007/\text{H}\beta$ line ratios and synthetic line ratio considered here it seems most likely that both the gas structures are comprised of oxygen enriched material. For the higher velocity structure which Steele et al. (2011) describes as a bipolar conical outflow this is consistent with the scenario of material being stripped from a CO white dwarf companion to the black hole, and driven to the observed velocity as an accretion-powered outflow. The added constraint of being oxygen enriched, does not, however place obvious constraints on the gas source for the lower velocity component.

As evidenced by the calculations summarized in Figure 5, the geometry of the emission region strongly influences the emission line ratios that it produces. As such the $[\text{O III}]\lambda 5007/\text{H}\beta$ ratio alone is insufficient to fully constrain the gas composition of the RZ2109 emission line system, or to positively identify the particular stellar type of the X-ray binary’s donor star. The WD donor star model is consistent with all the observations and calculations presented above. However we are not yet able to fully rule out other late stage or polluted stellar types with super-solar abundance atmospheres as the source for the observed outflow. With future observations of other spectral bands, including measurements of UV carbon lines CIV 1548 & 1551 Å and CIII] 1907 & 1910 Å, and more precise estimates of the emission line system’s gas mass, it may yet be possible to place tighter constraints on the emission line region’s composition and the X-ray binary source system.

M.M.S. and S.E.Z. wish to acknowledge support from NSF grant AST-0807557. Support for A.K.s work was provided by NASA through Chandra grant numbers GO1-12112X and GO0-11111A issued by the Chandra X-ray Observatory. K.L.R. acknowledges support from NSF Faculty Early Career Development grant AST-0847109. We thank the anonymous referee for the questions and critique which helped to strengthen the paper. We also thank Jack Baldwin for helpful discussion.

REFERENCES

- Ferland, G. J., Korista, K. T., Verner, D. A., et al. 1998, *PASP*, 110, 761
- Gnedin, O. Y., Maccarone, T. J., Psaltis, D., & Zepf, S. E. 2009, *ApJ*, 705, L168
- Ivanova, N. 2011, arXiv:1101.2864
- Kroupa, P. 2001, *MNRAS*, 322, 231
- Larsen, S. S. 2008, *A&A*, 477, L17
- Le Borgne, D., Rocca-Volmerange, B., Prugniel, P., Lançon, A., Fioc, M., & Soubiran, C. 2004, *A&A*, 425, 881
- Maccarone, T. J., Kundu, A., Zepf, S. E., & Rhode, K. L. 2007, *Nature*, 445, 183
- Méndez, R. H., Thomas, D., Saglia, R. P., et al. 2005, *ApJ*, 627, 767
- Peacock, M. B., Zepf, S. E., Kundu, A., et al. 2012, *ApJ*, 759, 126
- Prugniel, P., Soubiran, C., Koleva, M., & Le Borgne, D. 2007, arXiv:astro-ph/0703658
- Sarzi, M., Falcón-Barroso, J., Davies, R. L., et al. 2006, *MNRAS*, 366, 1151
- Shih, I. C., Maccarone, T. J., Kundu, A., & Zepf, S. E. 2008, *MNRAS*, 386, 2075
- Stanghellini, L., Shaw, R. A., Balick, B., et al. 2003, *ApJ*, 596, 997
- Steele, M. M., Zepf, S. E., Kundu, A., et al. 2011, *ApJ*, 739, 95
- Zepf, S. E., Maccarone, T. J., Bergond, G., Kundu, A., Rhode, K. L., & Salzer, J. J. 2007, *ApJ*, 669, L69
- Zepf, S. E., et al. 2008, *ApJ*, 683, L139

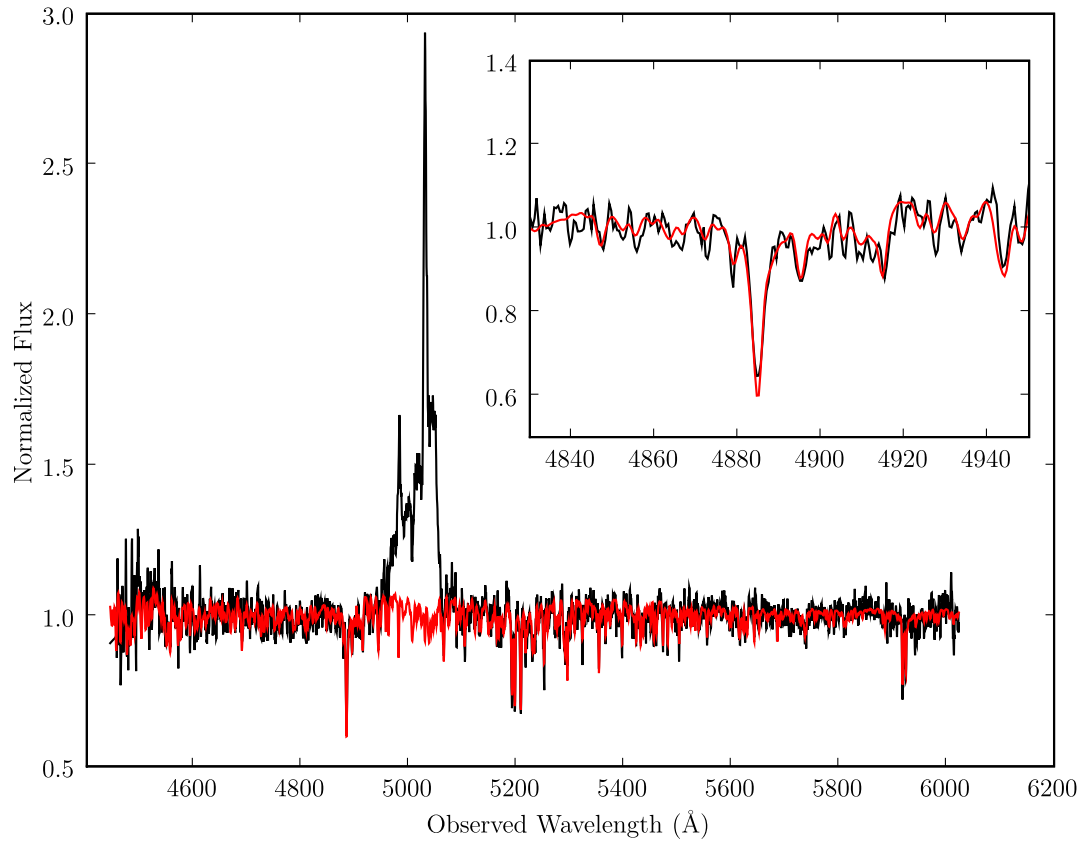


Fig. 1.— GMOS spectrum and the synthetic stellar component model. The GMOS observations of RZ2109 are shown using the black line. The gray line (red in the electronic version) depicts the best-fit synthetic stellar model. The inset shows the wavelength region surrounding $H\beta$ in detail.

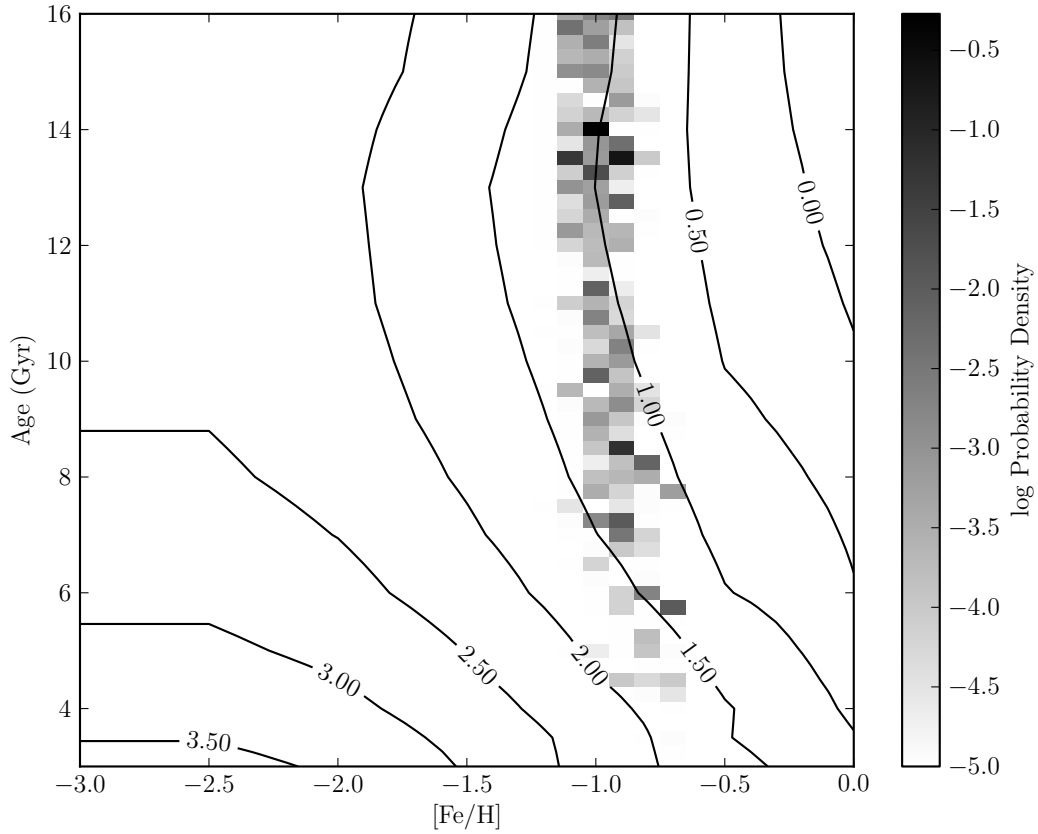


Fig. 2.— Stellar Model Fitting Uncertainties and $H\beta$ equivalent width contours. The gray scale grid displays the probability density in stellar parameter space that the stellar component of the RZ2109 spectrum would be determined to have a given set of parameters as described in section 3.1. The contour lines show the measurement of the $H\beta$ equivalent width with a 600 km s^{-1} aperture for a given stellar component model relative to the best-fit model, as described in section 3.2.

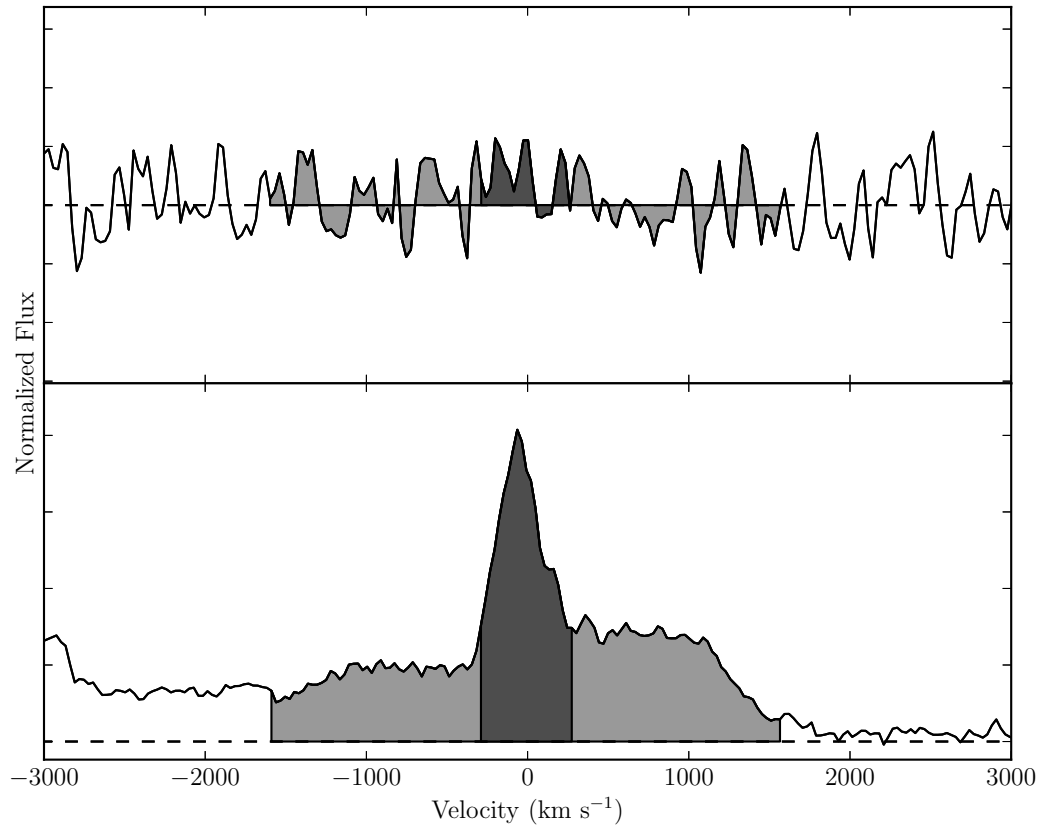


Fig. 3.— Equivalent Width apertures. The upper panel displays the $H\beta$ region of the stellar model subtracted GMOS spectrum in velocity space, and the lower panel gives the $[O\ III]\lambda 5007$ region. The 600 km s^{-1} aperture over which the equivalent width was measured is shaded with dark gray. The 3200 km s^{-1} aperture is shown in light gray. The dashed line gives the continuum level.

Table 1. Emission line equivalent widths and $H\beta$ ratios

Species	Rest Wavelength (\AA)	Aperture (km s^{-1})	EW (\AA)	X/ $H\beta$
H I	4861	3200	0.32 ± 0.32	1.0
		600	$0.21 \pm 0.13^{\text{a}}$	1.0
[O III]	5007	3200	33.82 ± 0.39	105.7
		600	13.14 ± 0.10	61.6

^aThe cited uncertainty reflects an 0.12 \AA observation measurement uncertainty and an 0.04 \AA stellar component model measurement uncertainty, which have been added by quadrature.

Table 2. Cloudy Model Grid Parameter Space

Mass Range (log g)	R_0 Range (log cm)	$\rho_H(R_0)$ (log cm^{-3})
31.1 – 31.4	18.3 – 19.0	4.2 – 5.3
31.5 – 33.5	17.8 – 19.0	4.5 – 5.5
33.6 – 34.2	17.8 – 19.0	4.4 – 5.7
34.3 – 35.3	17.8 – 19.0	4.5 – 5.5
35.4 – 35.7	18.2 – 19.0	4.0 – 4.4

Table 3. [O III] λ 5007/ $H\beta$ Ratio Limits

Confidence (%)	Aperture (km s^{-1})	Ratio, Upper $H\beta$ Limit	Ratio, Lower $H\beta$ Limit
68.3	3200	52.84	∞
90.0	3200	39.96	-163.9
95.0	3200	35.70	-110.1
99.0	3200	29.55	-67.06
68.3	600	41.05	165.4
90.0	600	33.04	7186.
95.0	600	30.17	-364.3
99.0	600	25.78	-119.3

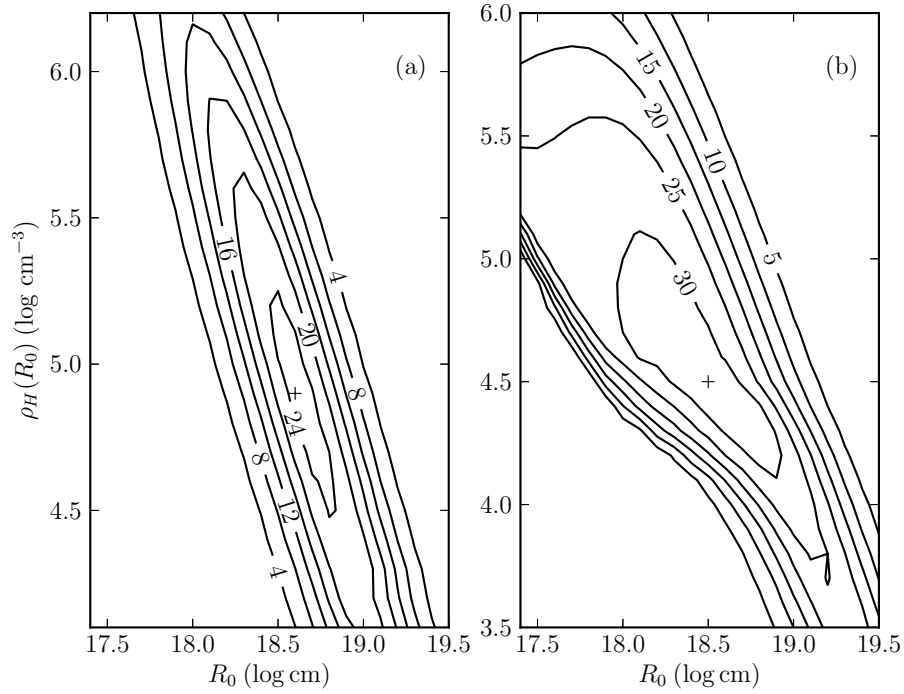


Fig. 4.— [O III]λ5007/Hβ ratio contours in Cloudy model parameter space of a solar composition gas. The Cloudy models depend on three free parameters: inner radius of the gas distribution (R_0), hydrogen density at the inner radius ($\rho_H(R_0)$), and total gas mass. Panel (a) shows the [O III]λ5007/Hβ ratio contours for 0.2 M_\odot gas mass. At this mass the maximum ratio of 26 occurs at position indicated by the cross. A maximum ratio of [O III]λ5007/Hβ =34 for all parameter space occurs for a gas mass of 100 M_\odot with contours for the other two free parameters shown in panel (b).

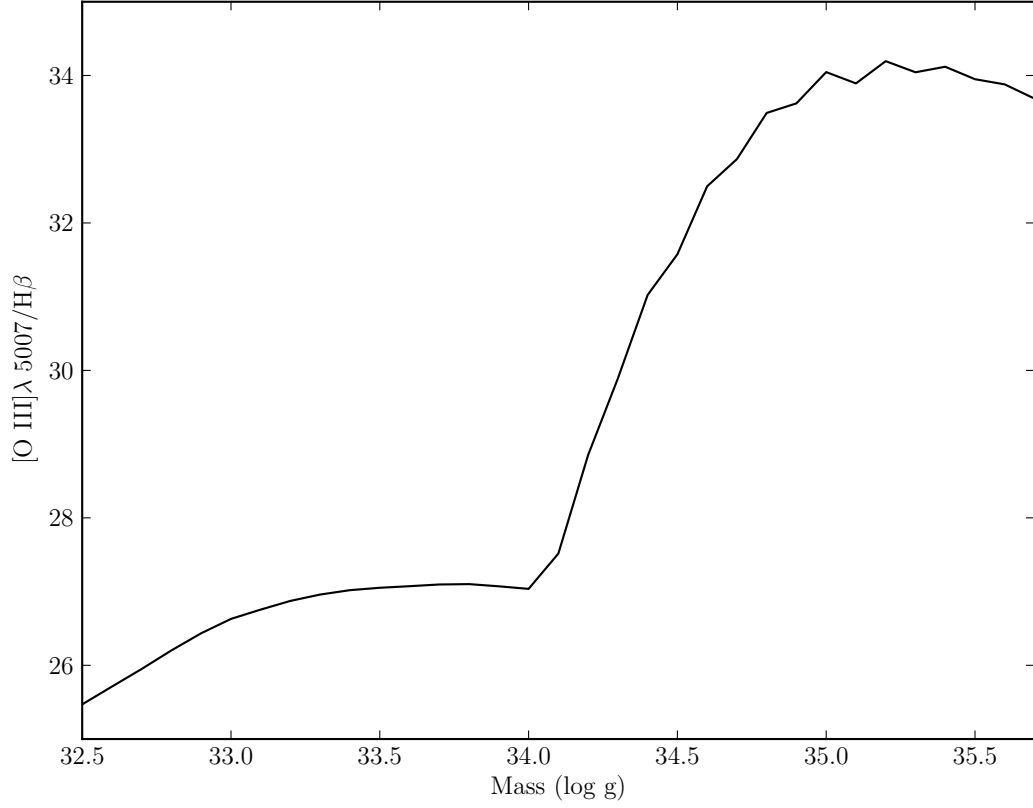


Fig. 5.— Maximum $[\text{O III}]\lambda 5007/\text{H}\beta$ ratios by gas mass. The trend-line depicts the maximum $[\text{O III}]\lambda 5007/\text{H}\beta$ ratio from Cloudy models for any given total gas mass, allowing the other free parameters (inner radius of the gas distribution and hydrogen density at the inner radius) to vary as necessary. The maximum ratio occurs with a total gas mass of $\sim 100 M_{\odot}$.